

## DYNAMICAL EVOLUTION OF VISCOUS DISKS AROUND BE STARS. II : POLARIMETRY.

X. HAUBOIS<sup>1,2,3</sup>, B. C. MOTA<sup>2</sup>, A. C. CARCIOFI<sup>2</sup>, Z. H. DRAPER<sup>4,5</sup>, J. P. WISNIEWSKI<sup>6</sup>, D. BEDNARSKI<sup>2</sup>, AND TH. RIVINIUS<sup>7</sup>

## ABSTRACT

Be stars exhibit variability for a great number of observables. Putting the pieces together of the disk dynamics is not an easy task and requires arduous modeling before achieving a good fit of the observational data. In order to guide the modeling process and make it more efficient, it is very instructive to investigate reference dynamical cases. This paper focuses on continuum polarimetric quantities and is the second of a series that aims to demonstrate the capacity of deriving the dynamical history and fundamental parameters of a classical Be star through the follow-up of various observables. After a detailed study of the different opacities at play in the formation of polarized spectra, we investigate predictions of polarimetric observables in the continuum for different dynamical scenarios. Our models are based on a coupling of a hydrodynamic viscous decretion simulations in a disk and a 3-D non-LTE radiative transfer code. Introducing the polarization color diagram (PCD), we show that certain combinations of polarimetric observables exhibit features that are characteristic of a mass loss history. This diagram also enables to estimate fundamental parameters such as the inclination angle, the disk density scale and the  $\alpha$  viscous diffusion parameter. We present the PCD as a powerful diagnosis tool to track the dynamical phases of a Be star such as disk building-up, dissipation, periodic and episodic outbursts. Finally we confront our models with observations of 4 Be stars that exhibited long-term polarimetric activity.

*Subject headings:* circumstellar matter — radiative transfer — stars: emission-line, Be — stars: individual ( $\pi$  Aquarii, 60 Cygni,  $\delta$  Scorpii and  $\psi$  Persei) — techniques: polarimetric

## 1. INTRODUCTION

Be stars are non-supergiant, early-type stars with a circumstellar (CS) disk that is created from matter ejected from the star. Recent observational facts brought by spectro-interferometry and spectro-astrometry (e.g. Meilland et al. 2012; Wheelwright et al. 2012) supports the fact that so far all studied Be star disks rotate in a Keplerian fashion. This characteristic, together with other observational signatures of the disk outlined in Carciofi (2011), are properties that only the viscous decretion disk (VDD) model can reproduce. This model, first suggested by Lee et al. (1991) and further developed by Bjorkman (1997), Porter (1999), Okazaki (2001), Bjorkman & Carciofi (2005) and Jones et al. (2008), among others, uses the angular momentum transport by turbulent viscosity to lift material into higher orbits, thereby causing the disk to grow in size. This model has already been successfully applied to systems showing stable continuum emission: e.g.  $\zeta$  Tauri (Carciofi et al. 2009),  $\chi$  Oph (Tycner et al. 2008) and  $\beta$  CMi (Wheelwright et al. 2012) and systems exhibiting a more variable photometric activity (28 CMa, Carciofi et al. 2012). In a recent review paper, Rivinius, Carciofi & Martayan (2013) discuss in detail the observational and theoretical evidences in support of the VDD

scenario for Be stars.

Polarization is a powerful tool to study the geometry of the disk (opening angle, flaring) of Be stars without angularly resolving it. Polarized flux originates from electron scattering off the disk, and is affected by both pre- and post-scattering absorption by H I atoms (Wood et al. 1996; Halonen & Jones 2013a). Since H I opacity depends on the physical state of the gas, studying polarimetric observables at different wavelengths allows one to probe different regions of the disk. In the literature, the polarimetric technique has an established history of providing a unique diagnosis in identifying and studying the detailed CS environments of Be stars (Wood et al. 1997; Carciofi et al. 2007, 2009; Wisniewski et al. 2010; Draper et al. 2011).

Haubois et al. (2012), hereafter Paper I, studied the temporal variability of Be disks, based on SINGLEBE VDD hydrodynamics simulations (Okazaki 2007). SINGLEBE solves the 1-D surface density evolution equation for a viscous isothermal Keplerian decretion disk. The effects of variable mass injection rates on the disk structure, and their corresponding effect on the photometry, were studied at different wavelengths and compared to observations. More specifically, we first studied the different timescales that characterize the evolution of the disk surface density and how this surface density responds to changes in the mass injection rates. These surface density profiles were used as inputs to the three-dimensional non-LTE Monte Carlo radiative transfer code HDUST (Carciofi & Bjorkman 2006, 2008) that allowed the calculation of photometric observables at various wavelengths. The characteristic shapes of these lightcurves agree qualitatively well with observations, which provide strong circumstantial evidence that viscosity is indeed the mechanism that redistributes matter along the CS disk. The first successful confrontation of theoretical VDD lightcurves with observations was done by Carciofi et al. (2012) for the Be star 28 CMa. To summarize, Paper I provides the reader with a description of the photometric variability from a Be star in

<sup>1</sup> LESIA, Observatoire de Paris, CNRS UMR 8109, UPMC, Université Paris Diderot, 5 place Jules Janssen, F-92195 Meudon, France, xavier.haubois@obspm.fr

<sup>2</sup> Instituto de Astronomia, Geofísica e Ciências Atmosféricas, Universidade de São Paulo, Rua do Matão 1226, Cidade Universitária, São Paulo, SP 05508-090, Brazil

<sup>3</sup> Sydney Institute for Astronomy, School of Physics, University of Sydney, NSW 2006, Australia

<sup>4</sup> Department of Physics and Astronomy, University of Victoria, 3800 Finnerty Rd, Victoria, BC V8P 5C2 Canada

<sup>5</sup> Herzberg Institute of Astrophysics, National Research Council of Canada, Victoria, BC V9E 2E7 Canada

<sup>6</sup> H. L. Dodge Department of Physics and Astronomy, University of Oklahoma, 440 West Brooks St Norman, OK 73019, USA

<sup>7</sup> European Organisation for Astronomical Research in the Southern Hemisphere, Casilla 19001, Santiago 19, Chile

TABLE 1  
STELLAR MAIN PARAMETERS USED IN THE SIMULATIONS.

Parameter	B0	B1	B2	B3	B4	B5
Mass ( $M_{\odot}$ )	14.6	11.0	8.6	6.1	5.1	4.4
Polar radius $R_{pole}(R_{\odot})$	12.8	9.6	7.5	5.4	4.5	3.8
Equatorial radius $R_{\star}(R_{\odot})$	5.8	4.9	4.3	3.6	3.3	3.0
$W^1$	0.53	0.53	0.53	0.53	0.53	0.53
$v_{rot}$ (km/s)	344	325	308	283	272	261
$v_{orb}$ (km/s)	648	613	580	534	512	492
$\Omega/\Omega_{crit}$	0.8	0.8	0.8	0.8	0.8	0.8
Oblateness	1.14	1.14	1.14	1.14	1.14	1.14
Polar temperature (K)	29 900	26 200	23 100	19 100	17 200	15 500
Luminosity ( $L_{\odot}$ )	24 200	10 200	4 400	1 500	830	467

<sup>1</sup>  $W = v_{rot}/v_{orb}$ , see Sect. 2.3.1 of Rivinius, Carciofi & Martayan (2013)

the framework of the VDD model. With the present paper, we aim at exploring the variability of the continuum polarimetric features in the same manner.

In §2, we describe the polarigenic mechanisms operating in Be disks. Then we present the dynamical models we investigated and their signatures on common continuum polarimetric observables. We also show the diagnosis potential of a series of diagrams that we named polarization color diagrams (PCDs) that represent a powerful tool to follow the mass injection history in Be stars (§3). Finally, a discussion and a comparison to observed data of these synthetic observables are presented in §4 before concluding.

## 2. POLARIZATION IN BE STAR DISKS

Continuum spectropolarimetric observations of Be stars usually reveal a sawtooth pattern that displays abrupt changes of the polarization close to the H I ionization thresholds (see, e.g., Quirrenbach et al. 1997, for examples of observed polarization spectra). It is useful to review the origin of this pattern to understand precisely the physical processes that control the shape of the polarized spectrum. In this Section, we therefore adopt an analytical model to describe a viscous decretion disk surrounding a rotationally deformed and gravity darkened star, see Table 1 for the adopted stellar parameters.

For the disk, we adopted the VDD model in its simplest form: after a sufficiently long and stable period of mass decretion, a viscous disk assumes a power-law density profile given by  $\rho = \rho_0 (R_{\star}/r)^{3.5}$  (Bjorkman & Carciofi 2005), where  $\rho_0$  is the density at the base of the disk. In this study and in the rest of the paper, we keep the disk outer radius fixed at  $20 R_{\star}$ . Thus, in this Section we explore the effects of two model parameters in the polarized spectrum: the spectral type of the star and the disk density scale.

Figure 1 shows two theoretical polarized spectra, at two different base densities and for an inclination angle of  $70^\circ$ . While the low density model has a nearly flat spectrum in the optical and near IR, the high density model displays a steep spectrum with marked changes in the H I ionization thresholds. This behavior can be understood in terms of the relative contribution to the total opacity of each opacity source. Figure 1 shows the total optical depth of the disk, measured in the radial direction along the midplane (orange lines). The contribution of the absorptive (free-free and bound-free) and scattering (Thomson) opacities are also shown.

At low density, the electron scattering opacity, which is wavelength independent, is responsible for most of the total opacity. The resulting polarized spectrum is consequently nearly flat. However, changes in the polarization level does occur close to H I ionization thresholds, more importantly

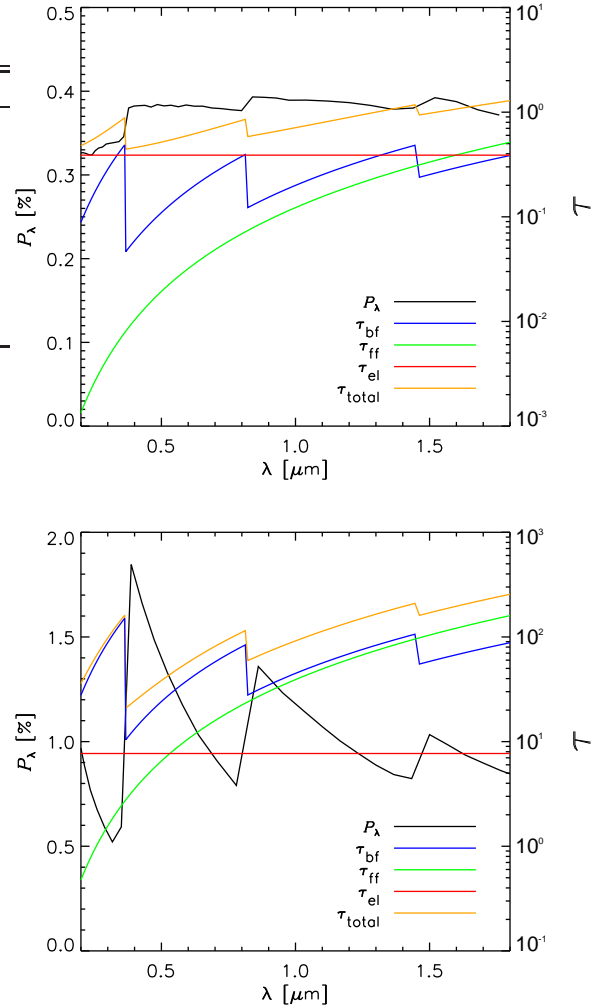


FIG. 1.— Polarized spectrum and radial optical depth contributions along the midplane. The total optical depth is the sum of the optical depth for each continuum opacity source, as indicated. Upper panel:  $4.2 \times 10^{-12} \text{ g cm}^{-3}$ ; lower panel:  $8.4 \times 10^{-11} \text{ g cm}^{-3}$ . The inclination angle is  $70^\circ$  and the spectral type is B2.

at the Balmer discontinuity ( $0.365 \mu\text{m}$ ). What causes the decrease in the polarization redward of the discontinuities is the increase in the H I opacity. This effect is thoroughly discussed in Wood et al. (1996), and can be understood in terms of pre-scattering (and to a lesser degree, post-scattering) absorption of starlight, that decreases the polarized flux and hence the polarization level, creating an anti-correlated aspect of the optical depth and polarization curves. If the density of the disk increases, the electron opacity will increase more or less linearly, as it is proportional to the number density of free electrons ( $\rho$ -diagnostics). However, the bound-free and free-free opacities, being roughly proportional to the square of the density (e.g., equation A1 and Eq. 30 of Bjorkman & Bjorkman 1994), will increase much faster than the electron opacity ( $\rho^2$ -diagnostics) so that, at high disk densities (lower panel of Fig. 1), the bound-free opacity dominates the total opacity. As a result, the polarized spectrum, besides displaying much more pronounced changes in the H I discontinuities, has a quite steep slope that results from the spectral dependency of the bound-free opacity.

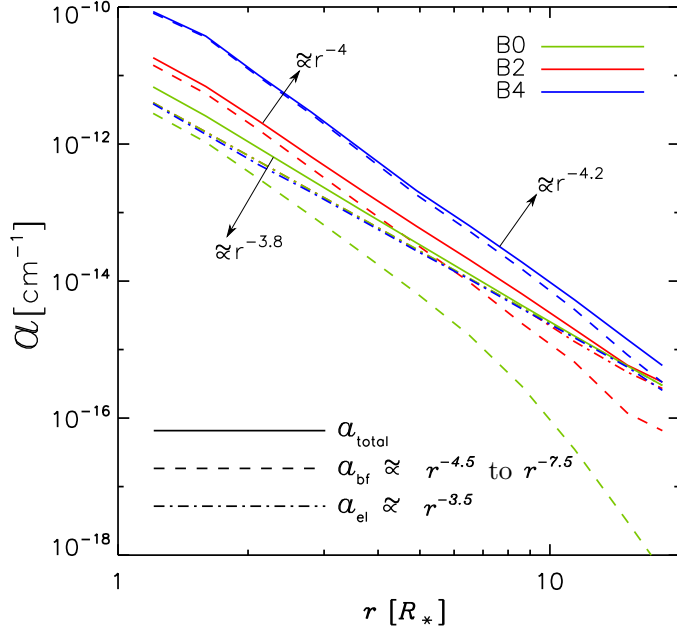


FIG. 2.— Absorption coefficient redwards of the Balmer discontinuity as a function of the distance to the stellar surface. The calculations assume a base density of  $\rho_0 = 8.4 \times 10^{-12} \text{ g cm}^{-3}$  and three spectral types: B0 (green curve), B2 (red curve) and B4 (blue curve). The free-free absorption coefficient is not shown because for short wavelengths it is much smaller than the other opacities. The electron scattering opacities are very similar for the three spectral types so that their curves overlap. Power-law indexes were estimated for the individual (in the legend) and total (on the graph) absorption coefficients.

In addition to the total radial optical depth, another important quantity in shaping the polarized spectrum is the radial dependence of the opacities or equivalently absorption coefficients. These are shown in Figs. 2 and A.1 for a wavelength redwards of the Balmer discontinuity. The effects of the spectral type on the absorption coefficients are shown in Fig. 2. The slope of the electron absorption coefficient curve,  $a_{\text{el}}$ , follows roughly the slope of the density ( $\propto r^{-3.5}$ ), because, for

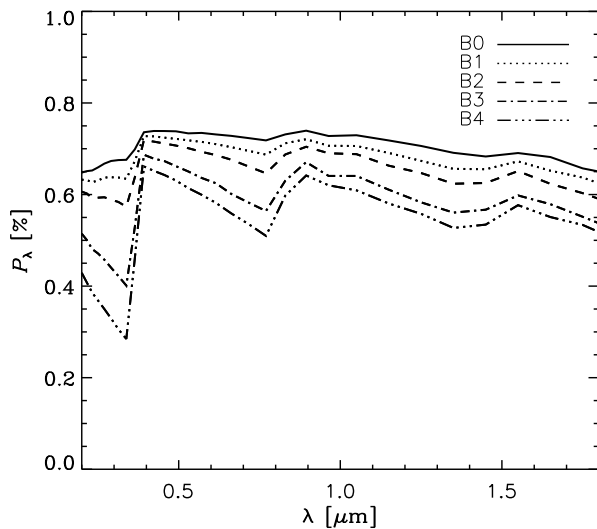


FIG. 3.— Polarized spectra for 5 spectral types: B0 (top curve) to B4 (bottom curve). The base density of the disk is  $8.4 \times 10^{-12} \text{ g cm}^{-3}$ . Inclination angle is  $70^\circ$ .

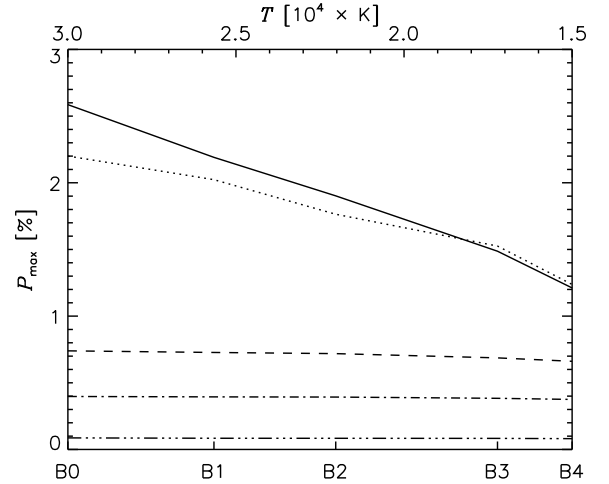


FIG. 4.— V-band maximum level of polarization versus the effective temperature of the star for five different base densities and five spectral types. The inclination angle is  $70^\circ$ . From top to bottom:  $8.4 \times 10^{-11} \text{ g cm}^{-3}$ ,  $4.2 \times 10^{-11} \text{ g cm}^{-3}$ ,  $8.4 \times 10^{-12} \text{ g cm}^{-3}$ ,  $4.2 \times 10^{-12} \text{ g cm}^{-3}$  and  $8.4 \times 10^{-13} \text{ g cm}^{-3}$ .

the models shown, H I is more than 98% ionized everywhere in the disk (in other words, the ionization fractions are close to unity and, therefore, the electron number density is roughly proportional to the total density). However, the bound-free absorption coefficient,  $a_{\text{bf}}$ , falls much faster than the electron absorption coefficient. For the B4 model, for instance,  $a_{\text{bf}} \propto r^{-4.5}$ , and no significant difference in slope was found for other spectral types (Fig. 2). The value of the radial slope of the bound-free opacity is controlled by the H I level populations, as shown in Appendix A. The actual values of the opacities differ quite markedly for different spectral types: the later the spectral type the larger the opacity. This is explained by the changing ratio between the ionizing UV luminosity vs. the total luminosity. Since the electron opacity is essentially the same for the models shown in Fig. 2, the large differences in the bound-free opacity implies that the dominant opacity source is different for each spectral type. So, for a B0 star, electron scattering dominates at  $0.3647 \mu\text{m}$  everywhere in the disk, and the opposite is true for the B4 star. An intermediate behavior is seen for the B2 star model: while the bound-free absorption coefficient dominates in the inner disk (up to  $\approx 6 R_*$ ), the opacity is controlled by electron scattering in the outer disk.

The resulting effects of the spectral type on the continuum polarization can be seen in Fig. 3. The polarized spectrum goes for a relatively flat one for the B0 star (electron scattering dominated) to a steep one, with marked discontinuity at the H I thresholds, for a B4 star at the density considered (bound-free dominated). Another interesting aspect of Fig. 3 is the fact that the polarization level for a given wavelength increases with the effective temperature. This is seen more qualitatively in Fig. 4 that shows how the V-band maximum polarization of a given model (that happens for an inclination around  $70^\circ$ , Wood et al. 1996) varies with spectral type. For low densities, all models (including the ones for later spectral types) are electron scattering dominated, meaning that electron scattering opacity is larger than the bound-free opacity in the optical and near-IR continuum (see Appendix A, Fig. A.1,

for an example of how the different opacities changes with changing disk density). This explains why the low density curve in Fig. 4 is flat.

As larger densities are considered, two effects concur for the strong dependence of the maximum polarization with spectral type. i) the relative contribution of the bound-free opacity to the total opacity increases, and eventually it will become the dominating source of opacity in the optical continuum (e.g., bottom panel of Fig. 1). Since absorptive opacities decrease the polarization level due to pre- and post-scattering absorption, it follows that the latter spectral types, that are more bound-free dominated, will have lower polarization levels. ii) the total scattering mass of the disk decreases for latter spectral types. For instance, in the high density B2 model of Fig. 4 the ionization fraction is about 99%, while for the B4 model it is 91%. These combined effects are so important that the maximum polarization level of the high density B0 model is about 2.5 times larger than the B4 model (Fig. 4).

In the above the relevance of continuum absorption to both the polarization level and the slope of the polarized continuum was discussed. However, Wood et al. (1996) showed that other processes, such as multiple scattering and occultation by the central star, also concur to define the shape of the polarized continuum. These latter processes are not discussed here, but they are all self-consistently included in our calculations (Carciofi & Bjorkman 2006). In a recent paper Halonen & Jones (2013a) also studied the polarization from Be star disks. Based on a self-consistent treatment of the thermal structure of the disk, they performed a radiative transfer in a gaseous disk that feeds a Monte Carlo multiple scattering routine that provides polarization levels for different parameters. Even though a quantitative comparison was not attempted, their results shown on Fig. 1 are qualitatively similar to the ones we present in this paper.

We conclude that the polarization spectrum carries valuable information about the physical conditions in the circumstellar disk. The polarization level at a given wavelength depends primarily on the total scattering mass of the envelope (number of free electrons), while the "color" of the spectrum (its slope or, equivalently, the size of the polarization change across the H I ionization thresholds) depends on the H I bound-free opacity, which is a strong function of both the disk density and the spectral type. These two polarization features (polarization level and "color") thus carry complementary information. This will be further explored in the next Section, particularly through the examples of the polarization in the  $V$ -band (polarization level),  $P_V$ , and the polarization level ratio across the Balmer discontinuity (polarization "color"),  $P_{BD}$ .

### 3. DYNAMICAL SIGNATURES IN POLARIMETRY

In the last section, we set the stage for explaining the origin of polarized spectra from Be stars using a VDD model in steady state (constant mass decretion rate). However, Be stars are known to be highly variable, and a constant mass decretion rate is likely to be the exception rather than the rule. A much more common situation is a disk whose characteristics are time dependent, in response to variable disk injection rates. To model the polarized signature of a time-dependent VDD, we follow the same approach used in Paper I. In that paper, the photometric variability was studied in detail and it was shown that predictions based on simple, yet realistic, mass injection rate scenarios agree quite well with the correlations observed for both shell and Be stars (we refer the reader to the discussion in § 5 of Paper I). Here, our goal is

to extend that study to the two polarimetric features described in § 2: the polarization level in the  $V$  band, and the color of the polarized spectrum as measured either by the polarization change across a H I ionization threshold or by the slope of the polarized spectrum.

For the reader's benefit, we succinctly describe the procedures adopted here; full details are given in Paper I. Using the `SINGLEBE` code, different dynamical scenarios were built from a given coefficient of viscosity ( $\alpha$ , Shakura & Sunyaev 1973) and different histories of the mass injection into the disk: monotonic building-up and dissipation phases of the disk, periodic injection rates and episodic outbursts. From each hydrodynamic simulation, we obtained temporal series of surface density profiles for a given dynamical scenario. To transform these structural information into observables, we used the surface density profiles as input to the radiative transfer code `HDUST` for each epoch of the dynamical scenario we wanted to investigate. This 3-D Monte Carlo code produces a full spectral synthesis of a star+disk system with a non-LTE treatment of the level populations and gas temperature and produces output spectra for the Stokes parameters  $Q$  and  $U$ . Unless mentioned otherwise, the model parameters are the same as presented in Table 1 and Table 2 of Paper I. This model that we call hereafter "the reference model" simulates a B2 star with a disk base density of  $8.4 \times 10^{-12} \text{ g cm}^{-3}$ . Nevertheless, we also explored the base density and spectral type parameter space and the corresponding values are specified in the figure captions.

#### 3.1. Disk build-up and dissipation

##### 3.1.1. $V$ -band Polarization and Balmer Discontinuity

To understand the effects of different dynamical scenarios upon polarimetric observables we start with a case of an uninterrupted disk build-up and dissipation. The disk build-up is simulated using a constant mass injection rate. The simulation starts without any circumstellar material, and the disk is gradually fed with matter as time goes on. The dissipation is modeled starting with a fully-developed disk; mass injection is turned off, and the disk material slowly dissipates both inwardly (re-accretion onto the star) and outwardly. We refer the reader to Paper I for a detailed discussion on how the disk grows and dissipates, and the timescales involved.

To explore the two polarimetric features we mentioned at the beginning of the section, we plot in Fig. 5 the temporal evolution of  $P_V$  and  $P_{BD}$  defined as:

$$P_{BD} = \frac{P_{\lambda_{BD+}}}{P_{\lambda_{BD-}}} \quad (1)$$

where  $P_{\lambda_{BD+}}$  and  $P_{\lambda_{BD-}}$  are the polarization levels estimated at higher and lower-wavelength intervals of the Balmer discontinuity, respectively. Results are shown for two  $\alpha$  parameters and three inclination angles.

Understanding the build-up phase (upper panels of Fig. 5) is straightforward: the polarization level monotonically increases as the disk builds up, approaching a limit value after a time that depends on the  $\alpha$  coefficient. This limit value is associated with the fact that even though viscous decretion disks never actually reach steady state, in the case of steadily building disks their surface density approaches a  $r^{-2}$  profile when time goes to infinity (Paper I and references therein). The maximum of the polarization level does not happen for  $90^\circ$  but rather at around  $70^\circ$  (e.g., Wood et al. 1996). Indeed, at high inclinations, photons scattered in directions parallel to



TABLE 2  
TIME IN YEARS REQUIRED TO REACH 95% OF THE LIMIT  
VALUE FOR  $\alpha = 1$

Inclination angle (deg)	$T_{P_{BD}}$	$T_{P_V}$	$T_{Vmag}$
30	1.4	1.9	2.8
70	3.0	3.9	< 0.1
80	2.7	4.2	3.4
85	1.0	4.8	7.1
90	0.4	8.4	8.1

the disk plane are much more likely to be absorbed by the disk than photons scattered away from the disk.

The dissipation (lower panels of Fig. 5) is characterized by an increase of the  $P_V$  signal right after the mass injection has been set to zero (no more mass injected at the base of the disk). This somewhat counterintuitive behavior is explained by the fact that the (unpolarized) emission in the  $V$ -band decreases soon after the mass injection stops (see Paper I). However, the total polarized flux decreases less rapidly because it is produced in a bigger area in the disk (Rivinius, Carciofi & Martayan 2013). This causes the polarization fraction to increase. When a sufficient fraction of the disk mass has been dissipated, there is less and less electrons available for Thomson-scattering, the polarization fraction naturally decreases as it is the case for  $P_{BD}$ . These variations are also naturally  $\alpha$  and inclination angle dependent. Eventually, all the polarized signals reach the zero value, when the disk has dissipated all or almost all its scattering mass. As shown in Fig. 5,  $P_{BD}$  grows and decreases faster than  $P_V$  because the former quantity is a  $\rho^2$ -diagnostics (depending on the  $\tau_{bf}$  opacity) whereas the latter varies linearly with the density (depending on the  $\tau_{el}$  opacity.) Hence,  $P_{BD}$  responds much faster to changes in density. To further illustrate this point, Tab. 2 shows the timescales that  $P_V$  and  $P_{BD}$  need to reach 95% of their limit value for an uninterrupted 50 yearlong phase of building up (for  $\alpha = 1$ ). The same timescales for the  $V$ -band magnitude are also listed for comparison (taken from Paper I).

### 3.1.2. Polarization color diagrams (PCDs)

From Fig. 12 of Paper I, we can see the excess magnitude in different bands stem from different locations in the disk. As demonstrated in § 2, the same apply for polarimetric features studied in this paper, which probes different disk regions. This offers the possibility of tracking the variations of the local density at different locations in the disk. This fact therefore provides us with an interesting possibility of following viscous processes in Be disks through different dynamical phases such as dissipation, build-up or outburst phases. Particularly, it is useful to look at the correlation between the polarimetric features  $P_{BD}$  and  $P_V$ . This correlation was detected observationally in Be stars that underwent build-up and dissipation phases by Draper et al. (2011), which showed that the process of disk growth and dissipation is associated to a loop in a diagram that plots  $P_{BD}$  vs.  $P_V$ . We saw in Sect. 2 that these quantities respond differently to density changes and are produced in different loci in the disk (although these loci do overlap). We can generalize the concept of this diagram by plotting other combinations of polarimetric observables that also represent a polarized spectrum “color” as a function of polarization level. In analogy to color magnitude diagrams (e.g. Fig. 22 of Paper I), this kind of diagram allows us to follow the evolution of Be star disks. We hereafter name this

kind of diagram polarization color diagrams (PCD).

Examples of PCDs are shown in Fig. 6. The formation of these loops can be described as follows. When the mass injection starts,  $P_{BD}$  increases from the value 1 and faster than  $P_V$  until it reaches a limit value as seen on Fig. 5. At the end of this first phase, the star has generated a large and dense CS disk. The formation path in the PCD corresponds to the upper part of the loops. When mass injection stops, the inner disk quickly reaccrues back onto the star; this causes a fast drop of  $P_{BD}$ , which being a  $\rho^2$ -diagnostics, responds fast to the density variations. However, as described in the previous section,  $P_V$  reacts more slowly to mass injections and increases a bit more until dissipation eventually makes its level drop. The curve then follows a track towards the bottom-left part of the diagram. What follows is a slow secular dissipation of the entire disk along which  $P_{BD}$  changes little and  $P_V$  diminishes steadily. The detailed shape of the loop depends on the viewing angle as shown in Fig. 6 and also on the value of  $\alpha$ .

To generate a PCD, we need to plot a quantity that measures the “color” of the polarized spectrum vs. the polarization level at some wavelength. Here, one can employ several quantities to measure the color; for instance, in addition to the polarization change in the Balmer discontinuity, other discontinuities can be used or, alternatively, the slope of the polarized spectrum can be measured directly from the ratio between the polarization values at different bandpasses. An example of different diagrams for the same model can be seen in Fig. 7 that compares the use of  $P_{BD}$  with the polarization change at the Paschen discontinuity ( $P_{PD}$ ) and the slope of the polarization spectrum as measured by the ratio between the polarization at the  $B$  and  $I$  bands ( $P_B/P_I$ ). All diagrams made according to this principle contain roughly the same information in the sense that they enable to track building-up and dissipation phases. For simplicity, from now on by PCD we refer to the diagram  $P_{BD}$  vs.  $P_V$ .

### 3.1.3. Diagnostic potential

Having described the two main features contained in the polarized spectrum (polarization level and color) and how these relate to the disk properties, we now explore the diagnostic potential of polarimetric observations of Be disks, with a focus on the usefulness of the PCDs. Figure 6 already showed that the shape of the loop in the PCD is very sensitive to the inclination angle of the system. Moreover, PCDs are characteristic of the density at the base of the disk and can be used to infer this quantity via VDD modeling. Figure 8 shows the different forms the PCDs can take depending on the density at the base of the disk. The amplitude of the loop in the PCDs is a clear signature of the base density: the loop has a bigger extent for a higher density, whatever the inclination angle. If the disk undergoes an almost constant building-up phase, the top region of the PCDs is reached in less than a year (for a viscous coefficient  $\alpha = 1$ ). Provided a few measurements typically spaced by one or two months and with  $\sim 0.1\%$  uncertainties, Fig. 8 shows that it is quite straightforward to disentangle between base densities that are different by a factor of 3 (except may be at the end of a long-term dissipation phase). We also note that the slope of the PCDs changes with density. For low densities the slope is smaller and the loop less broad, while for large densities the slope increases and the loop gets broader. This is a result of the different weight that H I opacity plays in each model.

Interestingly, PCDs exhibit a secondary loop for very high density models ( $> 1 \times 10^{-10} \text{ g cm}^{-3}$ ) seen close to equator-on

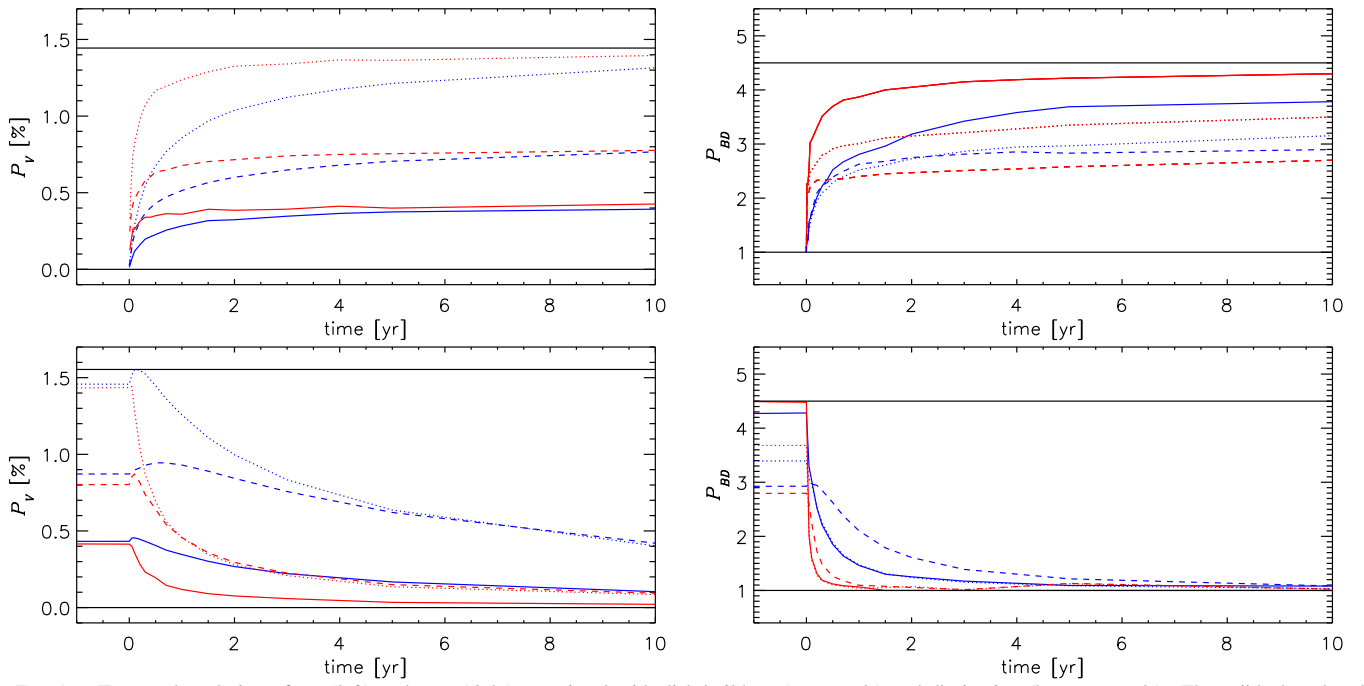


FIG. 5.— Temporal evolution of  $P_V$  (left) and  $P_{BD}$  (right) associated with disk build-up (top panels) and dissipation (bottom panels). The solid, dotted and dashed lines represent the lightcurves for inclination angles of  $30^\circ$  (face-on),  $70^\circ$  and  $90^\circ$  (edge-on), respectively. The blue and red colors represent models for  $\alpha=0.1$  and  $1.0$ , respectively. The solid black lines indicate the maximum values for each scenario. These curves were obtained using the reference model parameters.

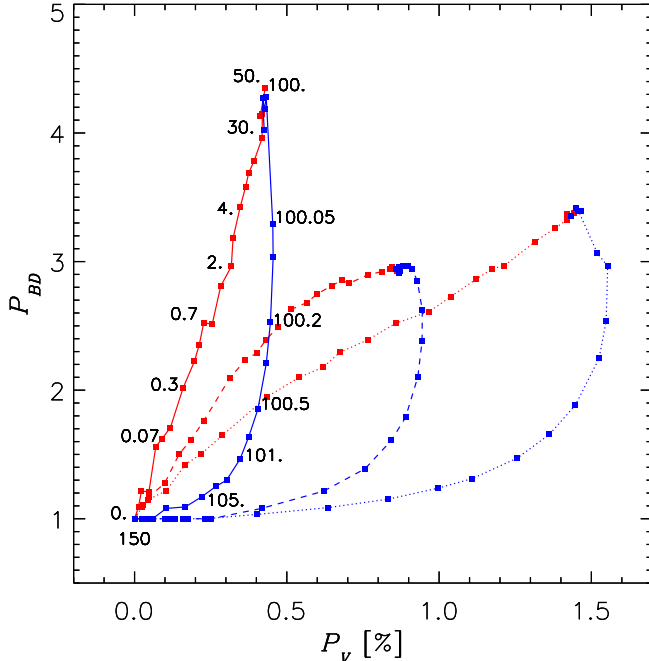


FIG. 6.— PCDs showing the process of disk growth and dissipation, involving a 100-year long building-up (in red) and 50 year dissipation (in blue). The results are shown for three inclination angles (solid line, 30°, dotted line, 70° and dashed line, 90°). For reference, epochs are marked in years along the curve obtained for 30° and  $\alpha=0.1$ . These curves were obtained using the reference model parameters.

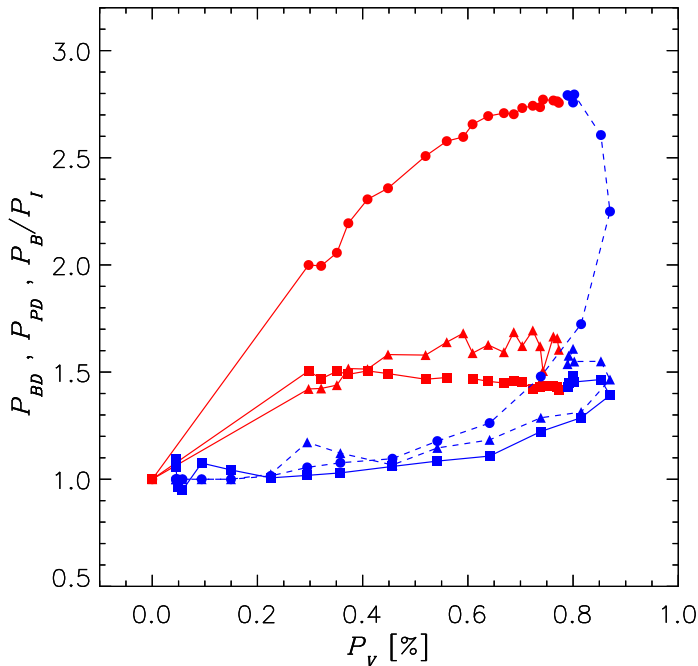


FIG. 7.— PCDs showing  $P_{BD}$  (filled circles),  $P_{PD}$  (squares) and  $P_B/P_I$  (triangles) as a function of  $P_V$ . The red curve shows a 50 year building up and the blue curve a following 50 year dissipation phase. Inclination angle is 90° and  $\alpha=1.0$ . These curves were obtained using the reference model parameters.

(Fig 9). For all the PCDs presented so far, the tip of the loop roughly corresponded to the end of the disk build-up phase (for instance, see Fig. 6). This is easily understood from the

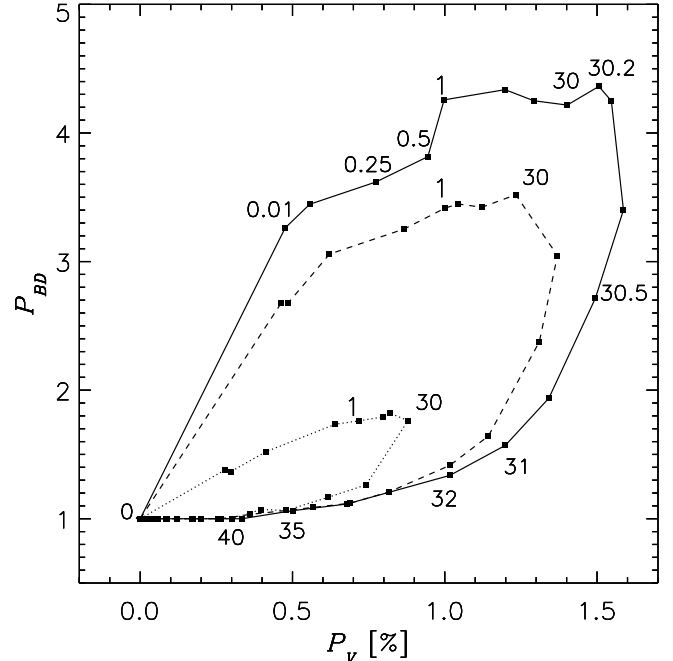


FIG. 8.— PCD for the reference model with 3 different base densities:  $6 \times 10^{-11} \text{ g cm}^{-3}$  (solid line),  $3 \times 10^{-11} \text{ g cm}^{-3}$  (dashed line) and  $1 \times 10^{-11} \text{ g cm}^{-3}$  (dotted line). The dynamical scenario involves a B3 star and 30 years of building-up followed by 30 years of dissipation. The inclination angle is 85° and  $\alpha=1.0$ . The epochs are marked and counted in years for the highest density model. The 1-year and 30-year epoch are marked for the three models.

fact that the higher the density, the higher the polarization change across the Balmer jump (e.g., Fig. 1). However, for the models shown in Fig. 9, the tip of the loop (labeled point 1) no longer corresponds to the end of the build-up phase (labeled point 2). This phenomenon is characteristic of high inclination angles ( $i > 80 \text{ deg}$ ) and the most likely explanation is a rather complex interplay between pre- and post-scattering absorption. Indeed, the two effects cause both a decrease in the polarization value and a change in the color of the polarized spectrum. However, pre-scattering absorption depends on the conditions of the innermost part of the disk, whereas post-scattering absorption follows the conditions at much larger radii. We thus explain Fig. 9 as follows: For the onset of the disk formation to point 1, the loops follow a normal behavior: as time passes  $P_{BD}$  grows as a result of the density increase everywhere in the disk. As the disk continues to grow and to get denser, post-scattering absorption starts to play a role in lowering  $P_{BD}$  (point 1 to 2). The track between point 1 and 2 in Fig. 9 thus indicates the growing role of the outer disk in absorbing the polarized flux coming from the innermost parts of the disk. When mass injection stops (point 2),  $P_V$  increases for reasons already explained in § 3.1, and  $P_{BD}$  also increases due to the smaller post-scattering absorption. At point 3, post-scattering absorption becomes negligible and, at the same time, the  $P_{BD}$  also drops due to the lack of density. This is why the  $P_{BD}$  level at the top of the secondary loop (point 3) is always smaller than the level at the top of the primary loop (point 1). Finally, the PCD follows a normal track towards  $P_{BD} = 1$  and  $P_V = 0$ , characteristic of an emptying disk. Moreover, since this post-scattering absorption changes the color of the polarized spectrum, the phenomenon we just described is more important for late spectral type stars where the polarization color is more pronounced. From the observa-

tional point of view this example shows that it is not possible to directly associate a value of  $P_{BD}$  to a disk density scale, at least for close to edge-on viewing.

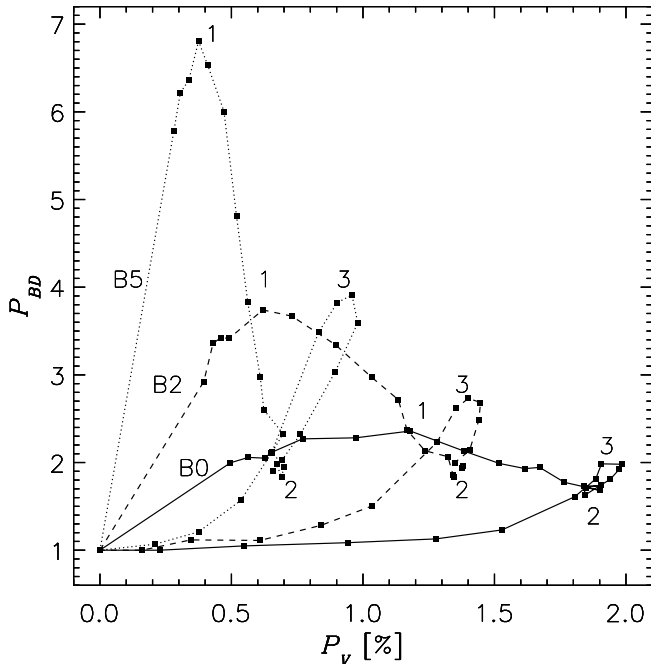


Fig. 9.— PCDs for 3 different spectral types (solid for B0, dashed for B2 and dotted for B5) with a dynamical scenario compound of 30 years of building-up followed by 30 years of dissipation. The base density is  $1 \times 10^{-10} \text{ g cm}^{-3}$ . The inclination angle is  $90^\circ$  and  $\alpha=1.0$ . Numbers indicate three reference times that help describing the disk evolution in the text. Whereas 1 and 3 represent different epochs depending on the spectral type, the number 2 always marks the stop of mass injection in the disk at  $t = 30$  years.

Fig. 4 showed how the maximum polarization of a given model depends on  $T_{\text{eff}}$ . A strong dependence of the PCD on the central star spectral type is thus to be expected. On Fig. 10, we can see that the spectral type impacts the PCD in various ways. Firstly, the range of  $P_V$  values plotted in the PCD increases with increasing  $T_{\text{eff}}$  (in agreement with Fig. 4). Secondly, the slope of the PCD increases with decreasing  $T_{\text{eff}}$ . This again can be understood in terms of the relative importance of electron scattering opacity vs. H I opacity.

As seen above, the higher the effective temperature, the lower the bound-free opacity for a given density. Also, the lower the bound-free opacity, the smaller the polarization change across the Balmer discontinuity. Therefore, the slope of the loop in the PCD is a good tracer of the bound-free opacity. In view of the results shown in Figs. 8 and 9, the diagnostic potential of the PCD as a measure of the disk density depends critically on a good determination of the spectral type of the central star.

Halonen & Jones (2013a) studied the shape of the PCD loops using add hoc models that simulated the disk growth and dissipation by simply changing the inner and outer radius of the disk while keeping the density slope fixed to its steady state value ( $n = 3.5$ ). A quantitative agreement between this work and their results is not to be expected due to the different disk models used but also because their definition for  $P_{BD}$  is based on the difference between polarization levels before and after the Balmer discontinuity instead of the ratio (definition

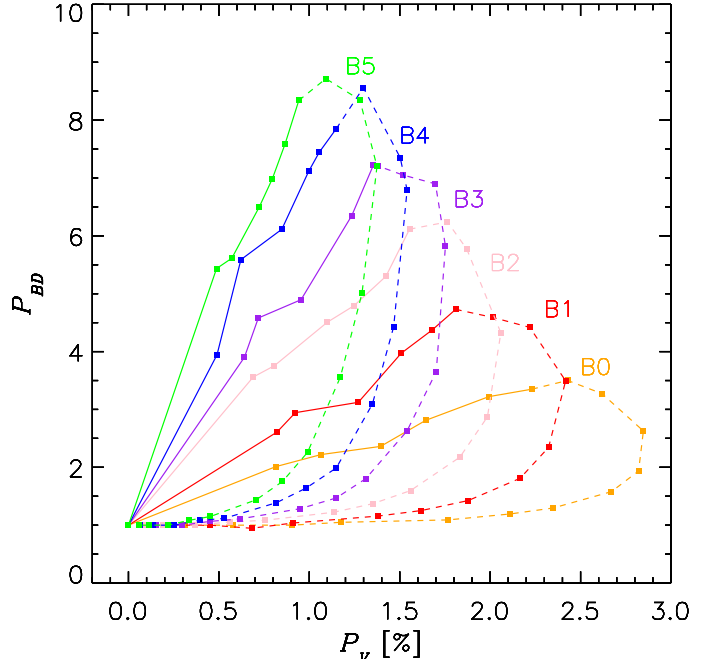


Fig. 10.— PCD for a central star of different spectral types, as indicated. The scenario is the same as for Fig. 8. The solid lines mark the build-up phase whereas the dashed lines represent the dissipation phase. The base density is  $6 \times 10^{-11} \text{ g cm}^{-3}$ . The inclination angle is  $70^\circ$  and  $\alpha=1.0$ .

used in the present work).

### 3.2. Periodic mass loss rate

The previous section dealt with the case of a disk forming when none exists and the dissipation of a fully formed disk. This situation has been already observed in several Be stars. Some examples include  $\pi$  Aqr (a well-documented disk dissipation that started in 1986 can be found in Wisniewski et al. 2010) and the disk growth of  $\omega$  Ori in the eighties (Sonneborn et al. 1988). In between these limiting cases, most Be stars display either an irregular variability, or, what is more rare, a quasi-cyclic variation of the light curve (Sabogal et al. 2008). The best-studied example of the latter case is  $\omega$  CMa, that displays 2–3 yr long outbursts separated by 4–5 yr of quiescence (Štefl et al. 2003). In this section we explore what is the polarization signature expected when the mass injection is turned on and off periodically.

A periodical scenario is defined by three parameters: the mass injection rate, the period, and the duty cycle, which indicates the fraction of time in each cycle where mass injection rate is larger than 0 (see Paper I for details). Figure 11 shows the temporal evolution of  $P_V$  and  $P_{BD}$  for a periodical mass injection scenario (6-yr period and 50% duty cycle, meaning that mass is continuously injected into the disk for three years every six years). The main difference between this case and the scenarios seen in § 3.1 is that the disk doesn't totally build and dissipate. The lowest values of  $P_V$  and  $P_{BD}$  at the end of quiescence are therefore different from 0% and 1, respectively, and the maximum values are less than for an uninterrupted building-up phase (Fig. 5). Figure 12 compares the tracks in the PCD of a periodical scenario (1-yr period, 50% duty cycle, dashed curve) to that of a fully formed disk (formation from no previous disk followed by full dissipation, solid curve). The latter case forms a closed loop with maximal



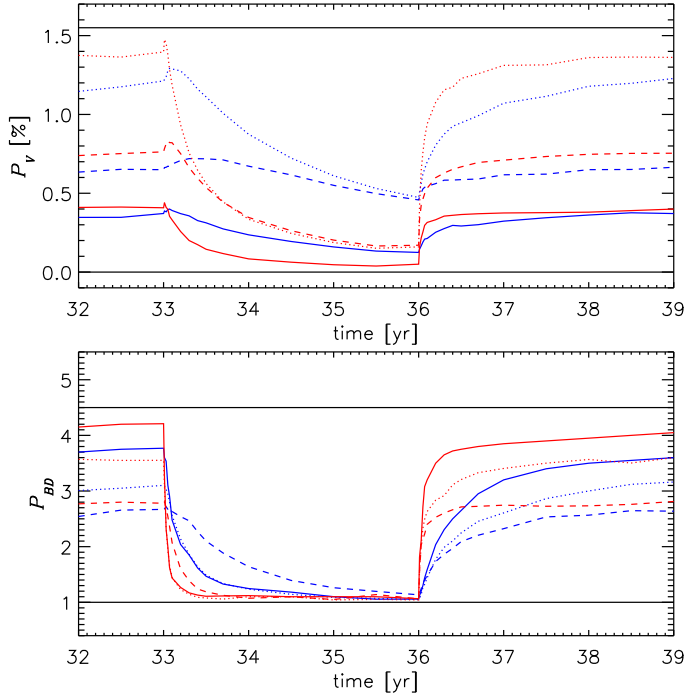


FIG. 11.— Same as for Fig. 5 for the 6th cycle of a periodic mass injection scenario with period of 6 years and a duty cycle of 50%. The solid black lines indicate the limit values that are reached for uninterrupted build-up and dissipation phase.

extent because at the end of the build-up phase the disk density approaches a limit value (Paper I), and at the end of the dissipation the disk matter has been almost completely lost. In the case of a periodical mass injection, however, there are three main differences: i) the cyclic mass injection prevents the disk density to reach its limit value, ii) at the end of quiescence the disk matter has not yet been fully lost, and iii) a given cycle starts with matter already accumulated in the previous one, so the total disk mass of each successive cycle, at a given phase, is always larger than the previous ones. Observationally, we already saw on Fig. 11 that these differences imply that the variations of  $P_V$  and  $P_{BD}$  will be of a smaller amplitude but it also results in a variation of these curves from cycle to cycle. This last point depends on the parameters of the scenario and is mainly visible for low-period scenarios (i.e. about a year or less for  $\alpha = 1.0$ ). This is well illustrated in Fig. 12: the loops in the PCD for a periodic scenario never close, and they are of a smaller amplitude than the loops for fully formed and dissipated disks in which they are confined.

### 3.3. Episodic mass loss rate

The most common type of variability observed in Be stars is of an irregular nature, which means that the mass injection rate varies with time in a complicated way. One extreme example are the so-called “flickering activity”, which is related to short-term variations seen in several observables. Examples of flickering activity can be found in Rivinius et al. (1998) ( $\mu$  Cen, photometry and spectroscopy) and Carciofi et al. (2007) ( $\alpha$  Eri, polarimetry). The “flickering” is attributed to an enhanced mass injection rate (outburst) that lasts from a few days to several weeks.

To illustrate what are the effects of an outburst in the polarimetric features, Fig. 13 shows a PCD for a dynamical scenario involving a 20-year long building-up phase followed by

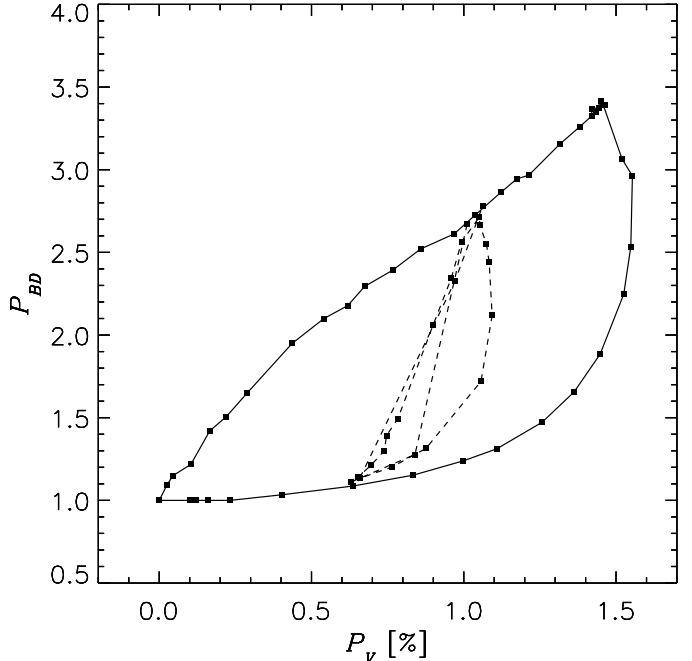


FIG. 12.— PCD at  $70^\circ$  of inclination angle and with  $\alpha = 0.1$  for the same dynamical scenario shown in Fig. 6 (in solid line) and for another one where the mass injection rate is periodically turned on and off every one year (in dashed line).

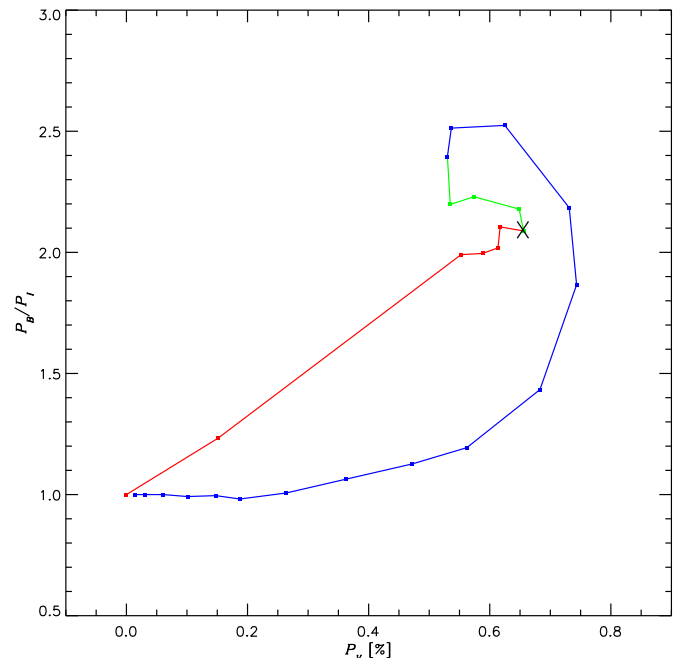


FIG. 13.— PCD showing  $P_B/P_I$  as a function of  $P_V$  for a 0.2 year outburst ( $\dot{M} = 3.3 \times 10^{-8} M_\odot/\text{year}$ , green curve) following a 20 year-long ( $\dot{M} = 1.6 \times 10^{-8} M_\odot/\text{year}$ , red curve) stable period of building-up. The outburst is then followed by a 30 year dissipation (blue curve). The X point marks the start of the outburst. The parameters are those of the reference model (B2 star). The inclination angle is  $39^\circ$  and  $\alpha=1.0$ .

a 0.2 year outburst with a mass injection rate twice higher than for the previous phase. The outburst is then followed by a 30 year dissipation phase. The first 20 years of disk for-

mation displays the same signature in the PCD as seen above (red line in Fig. 13). After the mass injection rate doubles at  $t = 20$  yr, the disk density gradually increases inside-out (see Fig. 11 of Paper I for a description on how the disk density evolves with time in this scenario). The signature of the outburst (green curve in Fig. 13) in the PCD is quite curious: while  $P_B/P_I$  stays essentially the same,  $P_V$  initially decreases between epochs 20.01 and 20.1 years. This can be understood in terms of the sudden increase in the disk continuum emission (Fig. 21 of Paper I) as a result of the enhanced densities in the inner disk. After the disk total mass adjusts to the new mass injection rate ( $\dot{M} = 1.6 \times 10^{-8} M_\odot/\text{year}$  at epoch 20 years or so), then  $P_V$  increases again. After the end of the outburst, mass injection is turned off ( $t = 20.2$  yr) and the model follows a dissipative path in the PCD (blue curve), as seen before. The outburst thus adds an extra outgrowth to the loop compared to a dynamical scenario without any outburst and should be quite well-identified provided a sufficient time-coverage of polarimetric observations.

#### 4. COMPARISON OF THE PREDICTIONS WITH OBSERVED DATA

Long-term polarimetric observations of the Be stars 60 Cygni and  $\pi$  Aquarii were obtained with the spectropolarimeter HPOL and revealed several year long disk-loss episodes interrupted by outbursts (Wisniewski et al. 2010). PCDs made out of these measurement showed loop patterns whose general shape was generally well described with viscous disk build-up and dissipation phases (Draper et al. 2011). More recently, Draper et al. (2013) presented a polarimetric follow-up of 9 Be stars among which some of them exhibited very characteristic PCD patterns, similar to the ones we showed in the last section.

In this section, we compare our theoretical predictions with PCDs obtained from HPOL measurements for 60 Cygni,  $\pi$  Aquarii, and  $\psi$  Persei. We refer the reader to Draper et al. (2013) for further details regarding the observational data. Moreover, we also discuss polarimetric measurements of  $\delta$  Scorpii made with the IAG polarimeter at the Pico dos Dias Observatory (Bednarski & Carciofi 2012).

##### 4.1. $\pi$ Aquarii

The PCD of  $\pi$  Aqr presents a very clear observational evidence of a partial loop obtained during a  $\sim 180$  day polarimetric flare (Fig. 14, left panel). From a pre-existent disk ( $P_V = 0.9\%$ ,  $P_{BD} = 1.8$ ), the loop starts with a build-up phase until it reaches a maximum  $P_{BD}$  value of 2.2. After that, an irregular dissipation pattern (with small deviations probably due to short-lived mass injection events) is seen. As already reported in Draper et al. (2011) and in the present paper, the general clockwise loop is well explained by viscous processes. The exact PCD then depends on an interplay between the injected quantity of matter, the inclination angle, the  $\alpha$  parameter and a good knowledge of the disk state before the outburst. Such in depth analysis will be carried out in the future. However,  $\pi$  Aqr being a B1 type star (Slettebak 1982), the range of the observed  $P_V$  and  $P_{BD}$  values are consistent with the range of the values shown in Fig. 10. Since these latter correspond to maximum values obtained for full building-up and dissipation cases, we conclude the  $\pi$  Aqr polarimetric observations are compatible with our VDD predictions.

##### 4.2. 60 Cygni

60 Cyg presents a more complex case (Fig. 14, middle panel). The first part of the PCD loop forms a clear clockwise loop that is well understood with a classical building-up/dissipation scenario, albeit with an irregular shape, suggestive of possible events of mass injection into the disk. In this part, the slopes are quite high for a B1 spectral type star (Slettebak 1982) when one compares with Fig. 10. We speculate this could be a signature of a high base density (i.e., high mass injection rates) and/or low inclination angles. The remaining data points follow a quite irregular track in the PCD, displaying the enigmatic behavior of an increase of  $P_{BD}$  with a simultaneous decrease of  $P_V$ . The results of § 3.1 and 3.3 suggest possible ways to explain such a behavior (e.g., irregular mass injection rates), but the scarcity of the data points prevents any well-founded interpretation.

##### 4.3. $\delta$ Scorpii

$\delta$  Sco is a B0.2IVe star with an inclination angle of about  $35^\circ$  (Carciofi et al. 2006). A several-year-long campaign led at the Pico dos dias Observatory (LNA, Brazil) allowed to monitor the polarimetric activity of  $\delta$  Sco in the  $B$ ,  $V$ ,  $R$ ,  $I$  filters (Bednarski & Carciofi 2012). At JD  $\sim 2\,445\,500$ , the star was in a intermediary level of activity, having built a large disk in the course of the previous 10 years, when a photometric increase was observed in March 2010. Since the star is close to pole-on viewing, this increase is likely associated with a strong outburst (Paper I).

Polarimetric measurements were obtained before, during and after the march 2010 outburst (Fig. 14, right panel). In the PCD, the data shows the following chronological behavior:

- the  $P_V$  level decreases after the photometric outburst had started while the  $P_B/P_I$  level stays essentially the same,
- as the outburst proceeds, both  $P_B/P_I$  and  $P_V$  increases.

This behavior is qualitatively very similar to the outburst scenario described in Fig. 13. When an outburst happens on top of an already existing disk (which is the case for the 2010 outburst of  $\delta$  Sco), what is initially seen is a leftward track in the PCD, followed by an up-right track, characteristic of disk build-up and subsequent dissipation. The range of  $P_V$  levels are much lower than on Fig. 13 which could indicate that the  $\delta$  Sco disk was not in a very dense state. Even though no attempt is made here to fit the data, it is worth noting that the outburst scenario, as suggested by photometry (Bednarski & Carciofi 2012), is a quite attractive explanation for the unusual track in the PCD seen for  $\delta$  Sco, which, in turn, suggests that this track is consistent with a viscous disk scenario. This certainly deserves further scrutinization.

##### 4.4. $\psi$ Persei

Another observed PCD that we can compare to our models, especially with Fig. 9, is  $\psi$  Per (B5 star with a disk inclination angle of  $75 \pm 8^\circ$ , Delaa et al. 2011). Figure 15 represents a 15 year long polarimetric monitoring of this star. The first characteristic of this PCD is the gigantic variation seen in  $P_{BD}$  while  $P_V$  steadily increases over a period of 10 years, indicating that the disk is overall building up. The data point which is off scale corresponds to  $P_V \sim 0.5$  and  $P_{BD} \sim 80$ . Secondly, after  $P_{BD}$  decreased, a series of lower amplitude  $P_{BD}$  variations is seen (see zoom of Fig. 15), until both  $P_{BD}$  and

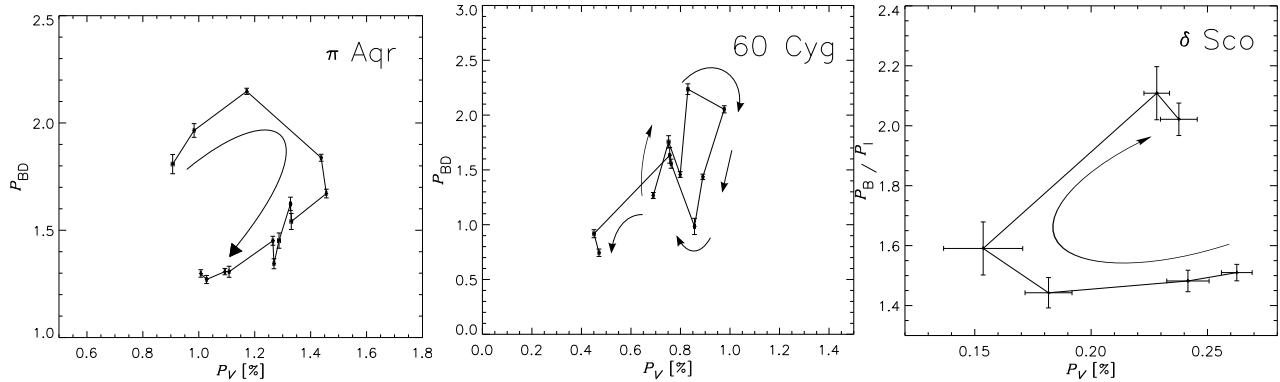


FIG. 14.— Observed PCDs of  $\pi$  Aqr (left panel) and 60 Cyg (middle panel), from Draper et al. (2013), and PCD of  $\delta$  Sco (right panel) made from measurements obtained at the IAG polarimeter. For the three PCDs, arrows indicate the chronological succession of epochs.

$P_V$  decline on a few month time length. The track that  $\psi$  Per follows on the PCD presents many similarities with the curve corresponding to the B5 spectral type on Fig. 9. Even though the time-scale and amplitude of the  $P_{BD}$  jump is not reproduced specifically by our model, the fact that a high  $P_{BD}$  variation is concomitant with a steady increase of  $P_V$  supports the fact that  $\psi$  Per was experiencing a building-up phase seen at a high inclination angle and with a very high disk density. We also mention that this peaky shape for a PCD is typical of late-type stars as shown in Fig. 9. Moreover, the zoomed panel of Fig. 15 also shows a pattern that is very similar to the counter-clockwise secondary loop in the PCD presented on Fig. 9. This type of behavior was only observed for models involving an inclination angle of  $i > 80^\circ$  and a base density higher than  $1 \times 10^{-10} \text{ g cm}^{-3}$ . However, we speculate that this sort of PCDs could be observed for lower inclination angles if the disk is denser ( $\rho_0 > 1 \times 10^{-10} \text{ g cm}^{-3}$ ).

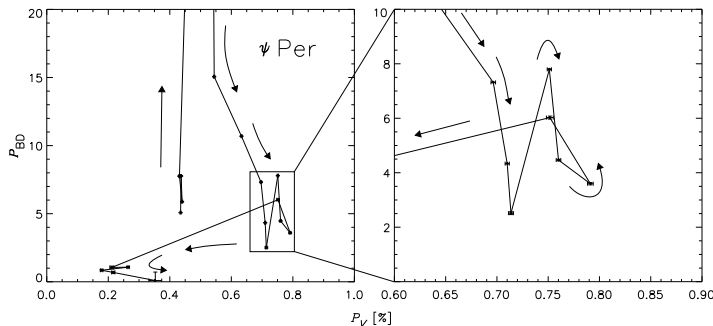


FIG. 15.— PCD of  $\psi$  Per built from HPOL observations that spanned 15 years.

It is important to mention that loop-shaped PCDs can also be qualitatively reproduced using spiral oscillation models as demonstrated in the Fig. 9 of Halonen & Jones (2013b). In this approach, a one armed density wave that is confined to a region extending out to  $10 R_*$  generate distinct shapes for the PCDs as well as characteristic signatures in the polarization angle variation. We conclude by saying that a detailed modeling specific to each observed Be star is needed to understand the origin of the polarimetric variability. PCDs and polarization angle measurements are critical observable quantities to disentangle a scenario involving a variable mass injection rate in an axisymmetric disk (with no polarization angle variation expected) from a scenario including a one-armed oscillation.

## 5. CONCLUSIONS

In this paper, we first review the mechanisms at the origin of the continuum polarization levels observed for Be stars under the assumption of a steady-state VDD model. For different disk densities and spectral types, we detail how the electron scattering, bound-free and free-free opacities shape the polarized spectrum. Analyzing further these opacities, we describe how they vary radially to establish the regions of the disk that are electron-scattering dominated and the regions that are bound-free dominated. For low densities (typically  $1 \times 10^{-12} \text{ g cm}^{-3}$ ), all models are electron scattering dominated and the polarization spectrum is roughly flat regardless the spectral type. For larger densities (typically greater than  $1 \times 10^{-11} \text{ g cm}^{-3}$ ), the bound-free opacity becomes the dominant opacity in the disk, at least in its innermost part. Based on this opacity description, we can define two polarimetric features that depend on different disk properties:  $P_V$ , the polarization level in the visible (or any other wavelength), is a measure of the scattering mass of the disk; and  $P_{BD}$  (the polarization change across the Balmer jump), a measure of the color of the polarization spectrum, which depends on the relative importance of the bound-free opacity to the total opacity. With a more realistic modeling based on a coupling of hydrodynamics and radiative transfer simulations, we show how these polarimetric features evolve with time for different disk mass injection scenarios. Different mass injection histories (constant, periodic or episodic) result in specific behaviors of the polarimetric observables. This led us to introduce an extension of the concept of BJV diagrams (Draper et al. 2011) that we named PCD (Polarization Color Diagram) as an analogy to color magnitude diagrams. The PCD plots  $P_{BD}$  (or other measure of the polarization color) versus the polarization level. PCDs constitute a powerful diagnosis tool to derive different physical parameters of the disk such as the inclination angle, the viscous coefficient  $\alpha$ , the disk base density and the spectral type of the central star on top of the mass injection history. Typically, the polarimetric features of a star evolving from a diskless phase (normal B star) to a Be phase (with a disk present) and back to a B phase will appear as a loop in the PCD, the upper part of the loop being associated with the disk construction and the lower part with the dissipation. In some particular cases of very high densities and high inclination angles, morphologic variations of the PCDs with the apparition of a secondary loop were found. Albeit the useful diagnostic potential, the morphologies seen in the PCD bear some degeneracy with respect to some parameters. For this

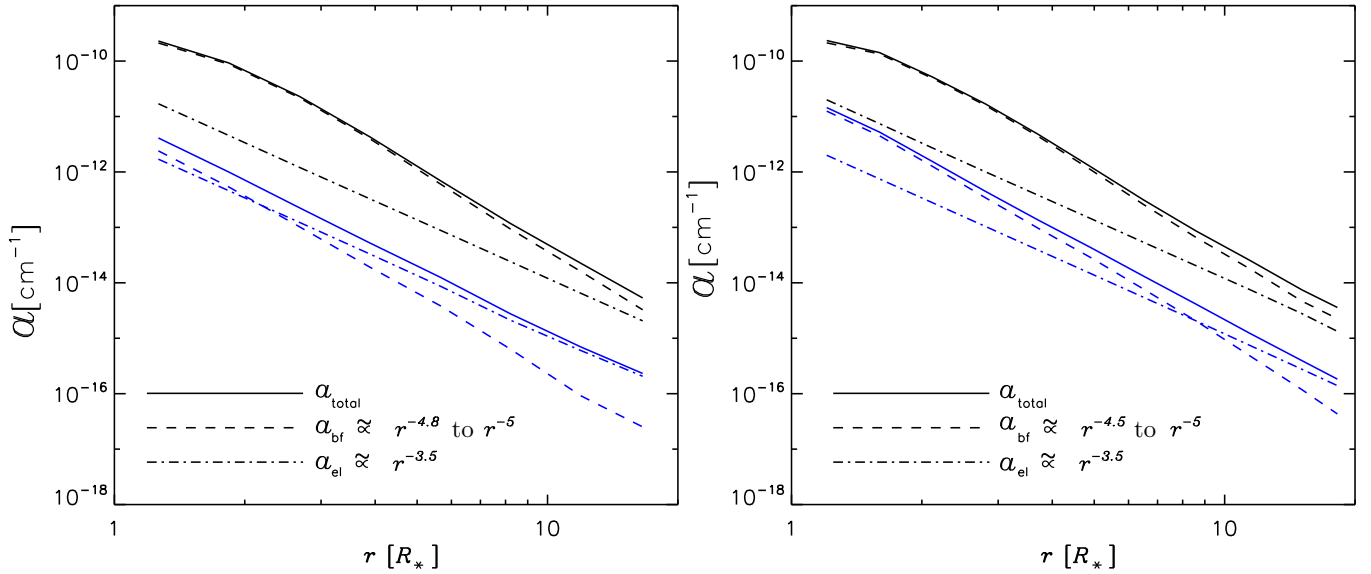


FIG. A.1.— Same as Fig. 2 for a B2 star (left) and a B3 star (right) and two different base densities:  $\rho_0 = 4.2 \times 10^{-11} \text{ g cm}^{-3}$  in black, and  $4.2 \times 10^{-12} \text{ g cm}^{-3}$  in blue.

reason, we stress that the more observables and the better time coverage, the easier to infer a dynamical scenario and physical parameters of the system. The theoretical predictions were confronted with observed PCDs of four stars. While  $\pi$  Aqr exhibits quite a clear building-up/dissipation pattern in its PCD, 60 Cyg presents a more irregular case that is likely to be the result of mass injection rate variations. We then analyse the PCD of  $\delta$  Sco and speculate that it probably represents the polarimetric counterpart of an outburst seen with photometry. Finally, we point out that the huge variations and the counter clockwise structure of  $\psi$  Per's PCD can be explained with our predictions for a B5 spectral type star, with a high inclination angle and a high density. However, a detailed modeling

remain to be carried out for each specific star to achieve an accurate reproduction of the observed PCDs.

XH thanks FAPESP for supporting this work through the grants 2009/07477-1 and 2010/19029-0. BCM acknowledges support from CNPq (grant 133338/2012-6). ACC acknowledges support from CNPq (grant 307076/2012-1) and Fapesp (grant 2010/19029-0). DB acknowledges support from CNPq (grant 134761/2012-0). This work has made use of the computing facilities of the Laboratory of Astroinformatics (IAG/USP, NAT/Unicisul), whose purchase was made possible by the Brazilian agency FAPESP (grant 2009/54006-4) and the INCT-A.

## APPENDIX

### THE RADIAL DEPENDENCE OF THE BOUND-FREE ABSORPTION COEFFICIENTS

Figure 2 showed that the radial dependence of the bound-free absorption coefficient is much steeper than the radial dependence of the density itself. A similar figure (Fig. A.1) compares how the scattering and bound-free absorption coefficients changes with changing density for two spectral types. It is interesting to note that the bound-free absorption coefficient becomes dominant on a larger extent of the disk for both base densities for later spectral types.

The radial dependence of the bound-free absorption coefficients in these two figures, consider the expression for the bound-free absorption coefficient in the Paschen continuum ( $\lambda_2 < \lambda < \lambda_3$ , where  $\lambda_2 = 3646 \text{ \AA}$  and  $\lambda_3 = 8203 \text{ \AA}$  are the H I  $n = 2$  and 3 photoionization thresholds). Taking into account, for simplicity, only the contributions of H I levels  $n = 2$  and 3 to the opacity (e.g., Bjorkman & Bjorkman 1994, Eq. 30)

$$a_{\text{bf}}(\lambda, r) = n(r) \left[ N_2 b_2 \left( \frac{\lambda}{\lambda_2} \right)^3 + N_3 b_3 \left( \frac{\lambda}{\lambda_3} \right)^3 \right], \quad (\text{A1})$$

where the photoionization cross sections are  $b_2 = 1.4 \times 10^{-17} \text{ cm}^{-2}$  and  $b_3 = 2.2 \times 10^{-17} \text{ cm}^{-2}$ ,  $n(r)$  is the particle number density, and  $N_2$  and  $N_3$  are the fractional occupation numbers of H I.

The H I occupation numbers of the same models shown in Fig. 2 and in the left panel of Fig. A.1 are plotted in Fig. A.2.  $N_3$  is much smaller than  $N_2$  everywhere in the disk, so, to a first approximation, the contribution of the atoms in this level (and above) can be ignored. Thus, the radial dependence of  $a_{\text{bf}}$  is thus controlled by the (explicit) radial dependence of  $n(r)$  and the (implicit) radial dependence of  $N_2$

$$a_{\text{bf}}(\lambda, r) \propto n(r) N_2 \propto r^{-(A+B)}, \quad (\text{A2})$$

where  $A$  is the slope of the density distribution and  $B$  is the radial variation of  $N_2$ . For a steady-state disk,  $A = 3.5$  (§ 2). The value of  $B$  is not constant, as is apparent from the fact that the  $N_2$  curves in Fig. A.2 are not straight lines. However, representative values



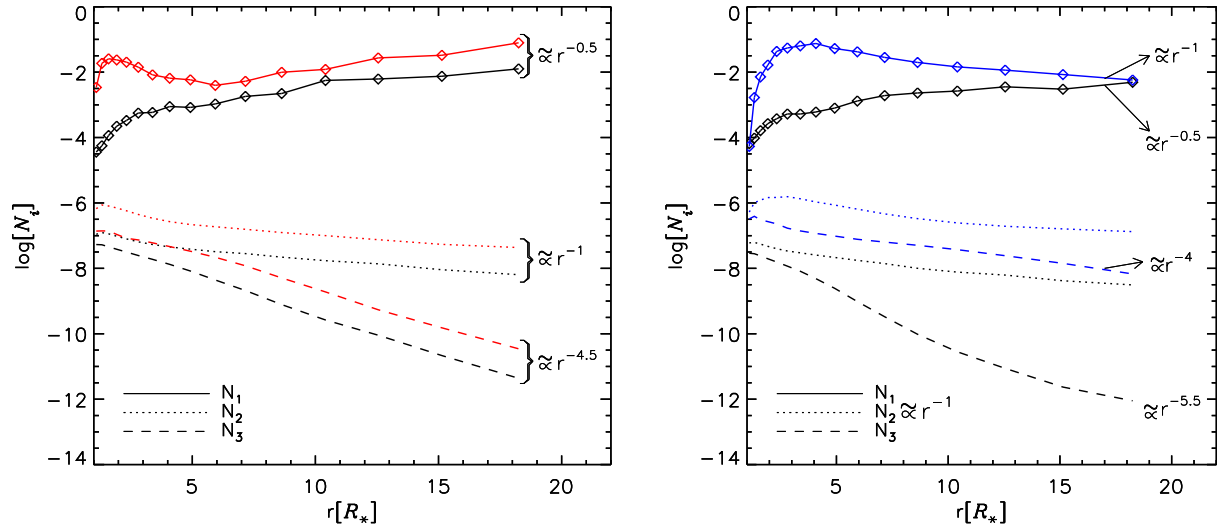


FIG. A.2.— Hydrogen level populations (up to level 3) vs. distance from the star. *Left*: Results for different spectral types (B2 in black and B4 in red) for a steady-state VDD with  $\rho_0 = 8.4 \times 10^{-12} \text{ g cm}^{-3}$ . *Right*: Results for different base densities ( $\rho_0 = 4.2 \times 10^{-12} \text{ g cm}^{-3}$ , black, and  $8.4 \times 10^{-11} \text{ g cm}^{-3}$ , blue) for a B2 star. Power-law indexes are indicated.

of  $B$  can be found by fitting the  $N_2$  with a power-law. The results, shown in Fig. A.2 gives  $B \sim 1$ . Thus,  $a_{\text{bf}}$  falls approximately as  $r^{-4.5}$ .

## REFERENCES

- Bednarski, D., & Carciofi, A. C. 2012, *Circumstellar Dynamics at High Resolution*, 464, 239
- Bjorkman, J. E., & Bjorkman, K. S. 1994, *ApJ*, 436, 818
- Bjorkman, J. E. 1997, *Stellar Atmospheres: Theory and Observations*, 497, 239
- Bjorkman, J. E., & Carciofi, A. C. 2005, *The Nature and Evolution of Disks Around Hot Stars*, 337, 75
- Carciofi, A. C., Miroshnichenko, A. S., Kusakin, A. V., et al. 2006, *ApJ*, 652, 1617
- Carciofi, A. C. & Bjorkman, J. E. 2006, *ApJ*, 639, 1081
- Carciofi, A. C., & Bjorkman, J. E. 2008, *ApJ*, 684, 1374
- Carciofi, A. C., Magalhães, A. M., Leister, N. V., Bjorkman, J. E., & Levenhagen, R. S. 2007, *ApJ*, 671, L49
- Carciofi, A. C., Okazaki, A. T., Le Bouquin, J.-B., Svtel, S., Rivinius, T., Baade, D., Bjorkman, J. E., & Hummel, C. A. 2009, *A&A*, 504, 915
- Carciofi, A. C. 2011, *IAU Symposium*, 272, 325
- Carciofi, A. C., Bjorkman, J. E., Otero, S. A., et al. 2012, *ApJ*, 744, L15
- Draper, Z. H., Wisniewski, J. P., Bjorkman, K. S., Meade, M. R., Haubois, X., Carciofi, A. C., Bjorkman, J. E., V 2011, *ApJ*, in prep
- Draper, Z. H., Wisniewski, J. P., Bjorkman, K. S., Haubois, X., Carciofi, A. C., Bjorkman, J. E., Meade, M. R., & Okazaki, A. 2011, *ApJ*, 728, L40
- Delaa, O., Stee, P., Meilland, A., et al. 2011, *A&A*, 529, A87
- Halonen, R. J., Mackay, F. E., & Jones, C. E. 2013, *ApJS*, 204, 11
- Halonen, R. J., & Jones, C. E. 2013, *ApJ*, 765, 17
- Halonen, R. J., & Jones, C. E. 2013, *ApJS*, 208, 3
- Haubois, X., Carciofi, A. C., Rivinius, T., Okazaki, A. T., & Bjorkman, J. E. 2012, *ApJ*, 756, 156
- Jones, C. E., Sigut, T. A. A., & Porter, J. M. 2008, *MNRAS*, 386, 1922
- Koubský, P., Harmanec, P., Hubert, A. M., et al. 2000, *A&A*, 356, 913
- Lee, U., Osaki, Y., & Saio, H. 1991, *MNRAS*, 250, 432
- Meilland, A., Millour, F., Kanaan, S., et al. 2012, *A&A*, 538, A110
- Okazaki, A. T. 2001, *PASJ*, 53, 119
- Okazaki, A. T. 2007, *Active OB-Stars: Laboratories for Stellar and Circumstellar Physics*, 361, 230
- Porter, J. M., & Rivinius, T. 2003, *PASP*, 115, 1153
- Porter, J. M. 1999, *A&A*, 348, 512
- Pringle, J. E. 1981, *ARAA*, 19, 137
- Quirrenbach, A., Bjorkman, K. S., Bjorkman, J. E., et al. 1997, *ApJ*, 479, 477
- Rivinius, T., Baade, D., Štefl, S., et al. 1998, *A&A*, 333, 125
- Rivinius, T., Carciofi, A. C. & Martayan, C., 2013, *A&A Rev.*, in press
- Rivinius, T., Carciofi, A. C., Štefl, S., Baade, D. & Bednarski, D., 2014, in preparation
- Sabogal, B. E., Mennickent, R. E., Pietrzyński, G., et al. 2008, *A&A*, 478, 659
- Shakura, N. I., & Sunyaev, R. A. 1973, *A&A*, 24, 337
- Sigut, T. A. A., & Jones, C. E. 2007, *ApJ*, 668, 481
- Slettebak, A. 1982, *ApJS*, 50, 55
- Sonneborn, G., Grady, C. A., Wu, C.-C., et al. 1988, *ApJ*, 325, 784
- Štefl, S., Baade, D., Rivinius, T., et al. 2003, *A&A*, 402, 253
- Tycner, C., Jones, C. E., Sigut, T. A. A., Schmitt, H. R., Benson, J. A., Hutter, D. J., & Zavala, R. T. 2008, *ApJ*, 689, 461
- Wisniewski, J. P., Draper, Z. H., Bjorkman, K. S., et al. 2010, *ApJ*, 709, 1306
- Wheelwright, H. E., Bjorkman, J. E., Oudmaijer, R. D., et al. 2012, *MNRAS*, 423, L11
- Wood, K., Bjorkman, J. E., Whitney, B., & Code, A. 1996, *ApJ*, 461, 847
- Wood, K., Bjorkman, K. S., & Bjorkman, J. E. 1997, *ApJ*, 477, 926
- de Wit, W. J., Lamers, H. J. G. L. M., Marquette, J. B., & Beaulieu, J. P. 2006, *A&A*, 456, 1027